Received: 15 February 2021 | Revised: 9 July 2021 | Accepted: 24 August 2021

DOI: 10.1111/jace.18133

Journal of the American Ceramic Society

RESEARCH ARTICLE

Reactive binder and aggregate interfacial zones in the mortar of Tomb of Caecilia Metella concrete, 1C BCE, Rome

Linda M. Seymour[1] | **Nobumichi Tamura**[2] | **Marie D. Jackson**[3] | **Admir Masic**[1]

[1] Department of Civil and Environmental Engineering, Massachusetts Institute of Technology, Cambridge, Massachusetts, USA

[2] Advanced Light Source, Lawrence Berkeley National Laboratory, Berkeley, California, USA

[3] Department of Geology and Geophysics, University of Utah, Salt Lake City, Utah, USA

Correspondence
Marie D. Jackson, Department of Geology and Geophysics, University of Utah, Salt Lake City, UT 84112-0102, USA.
Email: m.d.jackson@utah.edu
Admir Masic, Department of Civil and Environmental Engineering, Massachusetts Institute of Technology, Cambridge, MA 02139, USA.
Email: masic@mit.edu

Funding information
Department of Energy, Director of the Office of Science, Grant/Award Number: DE-AC02-05CH11231; Department of Energy, ARPA-E, Grant/Award Number: DE-AR0001139

Abstract

Integrated spectroscopic analyses and synchrotron X-ray microdiffraction investigations provide insights into the long-term reactivity of volcanic aggregate components and calcium-aluminum-silicate-hydrate (C-A-S-H) binder in mortar samples from the robust concrete of the sepulchral corridor of the Tomb of Caecilia Metella, 1st C BCE, Rome. The results of innovative micrometer-scale analytical maps indicate that Pozzolane Rosse tephra components–scoria groundmass, clinopyroxene, and leucite crystals–contributed to pozzolanic production of C-A-S-H binder and then remained reactive long after hydrated lime ($Ca(OH)_2$) was fully consumed. The C-A-S-H binding phase is reorganized into wispy halos and tendril-like strands, some with nanocrystalline preferred orientation or, alternatively, split into elongate features with short silicate chain lengths. These microstructures apparently record chemical and structural destabilization of C-A-S-H during excessive incorporation of Al^{3+} and K^{+} released through leucite dissolution. Resistance to failure may result from the intermittent toughening of interfacial zones of scoriae and clinopyroxene crystals with post-pozzolanic strätlingite and Al-tobermorite mineral cements and from long-term remodeling of the pozzolanic C-A-S-H binding phase. Roman builders' selection of a leucite-rich facies of Pozzolane Rosse tephra as aggregate and construction of the tomb in an environment with high surface and ground water exposure apparently increased beneficial hydrologic activity and reactivity in the concrete.

KEYWORDS
calcium (alkali) aluminosilicate hydrate (C-A-S-H) binder, post-pozzolanic processes, Roman architectural concrete, strätlingite, volcanic pozzolan

1 | INTRODUCTION

The Tomb of Caecilia Metella is a large concrete and dimension-stone circular drum built in 30–10 BCE at the third milestone of the Via Appia Antica.[1–3] The monument marks a pivotal transition from Republican era concrete construction in Rome to the highly sophisticated concrete architecture of the Imperial era (27 BCE through early fourth century CE) (Figure 1A, B). Faced with blocks of highly durable travertine, the circular tomb rests on a square base of concrete with coarse aggregate (*caementa*) quarried from the Capo di Bove lava flow (Figure 1B). Inside, a conical-shaped sepulchral chamber with an open oculus housed the body of Caecilia Metella, a member

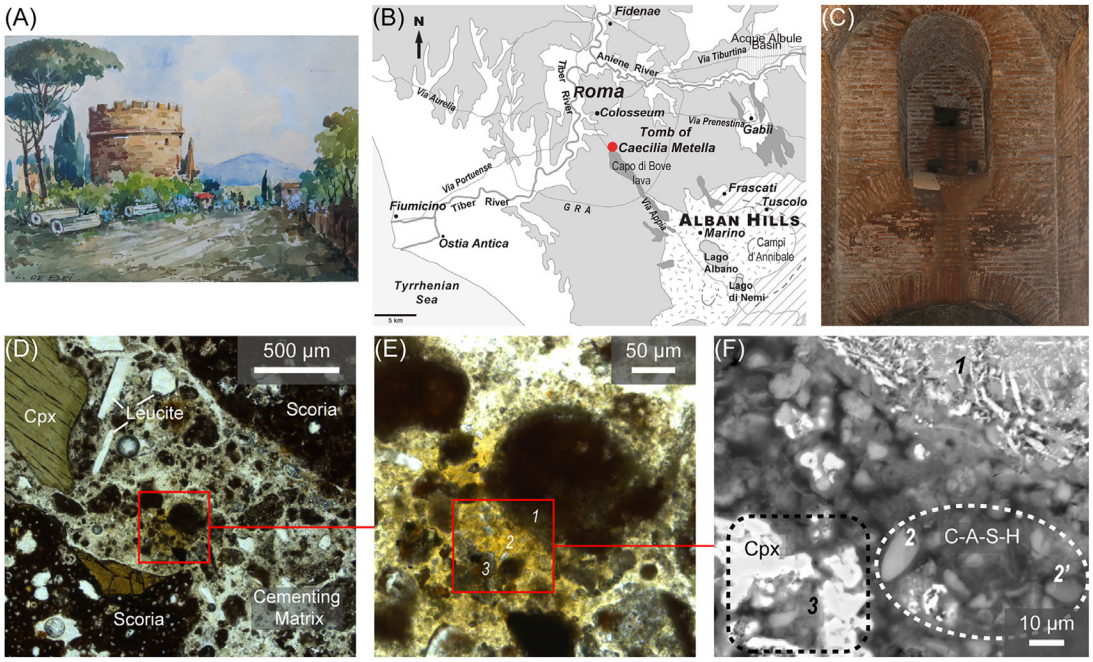

FIGURE 1 The Tomb of Caecilia Metella. (A) The cylindrical structure with the Colli Albani volcano in the background (L. de Bei, courtesy of A. Masic). (B) Geologic map showing location of the tomb at the tip of the Capo di Bove lava flow (after Jackson and Marra, reference 8). (C) Brick-faced concrete of the sepulchral corridor (M. Jackson). (D, E) Pozzolane Rosse tephra components in the mortar fabrics, plane polarized light (PPL) showing the interfacial zone of a microscoria (*1*), the C-A-S-H binding phase of the cementing matrix (*2*), and the altered rind of a clinopyroxene crystal (*3*) of the 06-CMETELLA-C2 mortar sample. (F) SEM-BSE image showing these features at higher magnification: acicular features in the interfacial zone (*1*), an altered C-A-S-H domain (*2*) and wispy features (*2'*) in the binding phase, and the diffuse border of the clinopyroxene (*3*) (see also Figure 4)

of the influential Caecilius Metellus family who married into the family of Marcus Licinius Crassus, one of the members of the first triumvirate in 59 BC with Julius Caesar and Pompey the Great;[4] the tomb may have been commissioned by her son.[1,3] The circular concrete structure, originally 21 m tall and 29 m in diameter, has walls 7 m thick that are open to precipitation through the oculus and to ground water penetration in the lower mortuary chamber.[1,5] Nevertheless, this structure preserves some of the most elegant and refined brick-faced concrete masonry of late republican Rome (Figure 1C). The concrete of the cylindrical wall remains highly cohesive despite 2050 years of exposure to infiltration of rain water, ground water, and high humidity.

The lower chamber of the tomb was excavated through deposits erupted from nearby Alban Hills volcano: the Capo di Bove lava and scoria (227±2 ka before present) and weakly consolidated tephra of the mid-Pleistocene Pozzolanelle pyroclastic flow (395±4 ka) (Figure 1B).[6,7] (A pyroclastic flow is a dense mass of hot tephra and gases ejected by an explosive pyroclastic eruption. Tephra is composed of vitric, crystal, and lithic particles.) The tephra used in the production of the highly cohesive mortar that binds the concrete in the lower chamber, however, was excavated from the Pozzolane Rosse pyroclastic flow (456±3 ka); the closest exposures are 0.5–0.75 km distant to the NW.[8] This voluminous eruption from Alban Hills volcano filled deep valleys eroded during Marine Isotope Stage 12 of the deep-sea $\delta^{18}O$ record[9] with thick deposits of tephra that subsequently underwent progressive alteration. There are three principal alteration facies with different authigenic mineral assemblages: superficial horizons that interacted with surface water producing a paleosol and greatest alteration facies, deeper horizons that interacted with ground water, producing a least altered facies and, in the intervening deposits, an intermediate facies of alteration.[10]

Roman builders of the second and early first century BCE employed alluvial deposits as aggregate in the mortars of concrete structures, as well as Pozzolanelle tephra and Pozzolane Rosse tephra, mainly the greatest alteration facies.[11,12] The mortar binds decicentimeter-sized rock aggregate to produce a conglomeratic concrete, described as *caementicia structura* by the Roman architect and engineer, Marcus Vitruvius Pollio, in about 30 BCE (*de Architectura* 2.4.1, 2.7.5). The volcanic tephra, or excavated sands (*harenae rubrae, nigra*, and *cana*), in these mortars were described by Vitruvius (*de Architectura* 2.6.1–2.6.6) and systematically correlated in Republican and Imperial era concrete structures by an astute Roman archaeologist, Esther

Boise Van Deman.[10,13,14] Van Deman described a transition to more cohesive, standardized mortars in late first century BCE "by Augustus, or by his predecessor Julius Caesar" as "an epoch in the history of concrete construction."[13,14] Concrete structural elements of the Tabularium (78 BCE) and Theater of Pompey[15,16] (55 BCE) record early innovations in advancing this technology.

Vitruvius wrote *de Architectura* for Octavian, who would become Emperor Augustus in 27 BCE; he was also a contemporary of Caecilia Metella. The concrete substructure of the Theater of Marcellus, constructed by Julius Caesar in 44 BCE, and the structure of the theater, constructed by Octavian mainly between 23 and 17 BCE, use the intermediate alteration facies of Pozzolane Rosse; the wall structures reveal some of the earliest brick-faced masonry in Rome.[11,17,18] The mortars have a robust cementing matrix with calcium-aluminum-silicate-hydrate (C-A-S-H) binder; strätlingite ($Ca_2Al_2SiO_2(OH)_{10}\bullet 2.25H_2O$)[19] mineral cements are also present.[11] A recent experimental reproduction of a nearly identical mortar fabricated at the Markets of Trajan about 140 years later indicates that C-A-S-H was produced pozzolanically through the reaction of hydrated lime ($Ca(OH)_2$) with Pozzolane Rosse components but that strätlingite formed only after calcium hydroxide was fully consumed.[20]

Touching on funerary structures exterior to Rome, Vitruvius gave guidance for building concrete walls that "over a long passage of time do not fall into ruins" (*de Architectura* 2.8.3–4): the walls should be "…two feet thick either of squared red stone (Tufo Lionato) or of brick (*bipedales parietes* or lava (*silicibus ordinariis*) laid in courses…" The architects of the Tomb of Caecilia Metella selected Capo di Bove lava *caementa* for the outer concrete structure and brick *caementa* with an interior fill of lava *caementa* for thick interior concrete walls.[1] The concrete construction of the tomb is one of the first examples of brick-faced concrete in Rome (*structura testacea*, *de Architectura* 2.8.18) and seems to intentionally implement best practices for funerary architecture.[1]

The concrete of the humid sepulchral corridor of the Tomb of Caecilia Metella[1,5] is exceptionally compact, with highly cohesive contacts between bricks and mortar and a general absence of macrocracks in the *opus testaceum* facing (Figure 1C). Roman builders selected the aggregate for the mortar from the least altered facies of the Pozzolane Rosse pyroclastic flow, which contains fresh clinopyroxene and leucite crystals and dusky red (10R 2/2 to 5R 3/4) to dark gray (N2) scoriae (Figure 1D, E). Alteration with ground water in the pyroclastic flow deposit produced surface coatings of translucent halloysite and opal and, occasionally, zeolites. Fine leucite crystals in scoria are commonly replaced by analcime but coarse leucite crystal fragments remain largely intact.[10,21]

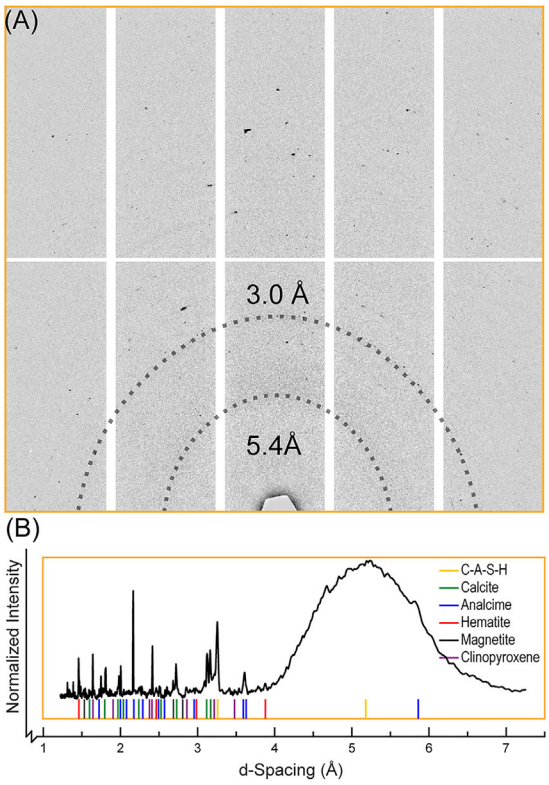

FIGURE 2 X-ray microdiffraction analysis of an intact C-A-S-H domain of the cementing matrix of the 06-CMETELLA-C1 mortar sample, *site 1a'* of Figure 3. (A) The diffuse reflections at 3.0 and 5.4 Å are distributed over χ, indicating that there is no preferred orientation (compare to Figure 3C). (B) The integrated intensity plot indicates calcite and primary and authigenic minerals associated with the neighboring microscoriae. Mineral assignments from RRUFF[34]

The central purpose of this article is to describe two mortar samples from the sepulchral corridor to gain insights into (1) the micrometer-scale processes that have contributed to high cohesion in the concrete and (2) how Roman builders' choice of volcanic aggregate influenced the micrometer-scale processes in the mortar that binds the concrete (see also reference 22). The complex C-A-S-H binder of the cementing matrix is described with synchrotron X-ray microdiffraction (μXRD) analyses (Figures 2 and 3) and scanning electron microscopy (SEM) (Figure 4). Next, the complex spatial and chemical relationships of interfacial zones of Pozzolane Rosse tephra components––scoria groundmass, clinopyroxene, and leucite crystals––in contact with this cementing matrix are described with correlative Raman spectroscopy, SEM, and energy dispersive X-ray spectroscopy (EDS) (Figures 5–7). The integrated analyses investigate whether the C-A-S-H binding phase has dissolved and/or undergone reconfiguration over the past 2000 years; whether dissolution of highly potassic leucite crystals produces

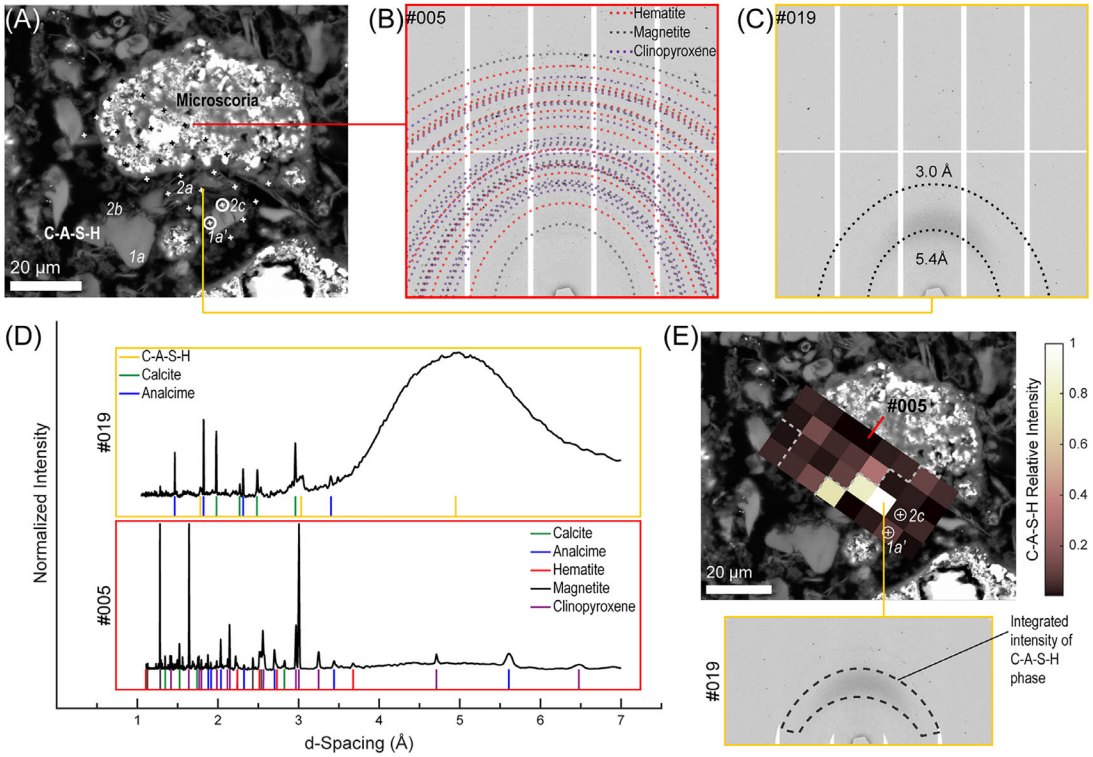

FIGURE 3 X-ray microdiffraction analyses of the cementing matrix of the 06-CMETELLA-C1 mortar sample. (A) BSE micrograph of Pozzolane Rosse microscoriae and C-A-S-H. (B) Debye diffraction plot (#005) showing clinopyroxene, magnetite, and hematite crystals in the microscoriae. (C) Debye diffraction plot (#019) of incipient elongate features in the binding phase with broad *d*-spacings centered at 3.0 and 5.4 Å. (D) Intensity integrated over 2θ reveals the breadth of the C-A-S-H reflections as compared to the crystalline phases in the microscoriae. (E) Integrated intensity over the region of C-A-S-H features (identified in lower panel) indicates the phase with nanocrystalline preferred orientation occurs predominantly in the interface of the scoria and cementing matrix at the location of the incipient elongate features. Mineral assignments from RRUFF[34]

potentially beneficial post-pozzolanic changes in the cementing matrix or, by contrast, the deleterious and expansive alkali silica gels that cause macroscale cracking in ordinary Portland cement (OPC) concretes;[23–25] and finally, how long-term changes in the interfacial zones of scoria, leucite, and clinopyroxene could further the cohesion of the mortar and refinement of microcrack surfaces (Figure 8) at a millennial time scale. The results provide a foundation for further investigations of the ancient binding phase and reactive interfaces in the Tomb of Caecilia Metella concretes. They also inform the development of innovative, environmental-friendly concrete infrastructure designed to replicate this long-term reactivity and to promote beneficial interactions between the hydrological environment and microstructural cementing processes.

2 | MATERIALS AND ANALYTICAL METHODS

The mortar samples were collected from the humid first century BCE concrete masonry of the Muñoz corridor in the lower structure of the Tomb of Caecilia Metella in 2006 (Figure 1C, see also reference 1). Figures 2–4 describe the 06-CMETELLA-C1 sample from the brick facing of the concrete wall, while Figures 5, 7, and 8 describe the 06-CMETELLA-C2 sample from the crest of the barrel vault of the Muñoz corridor.

2.1 | Sample preparation

Superglue™ adhesive and an embedding medium (Epo-Tek™ epoxy) were used in the preparation of the polished thin sections. Areas selected for synchrotron μXRD investigations were cut from the glass-mounted thin section with a precision saw. The 0.03-mm thick mortar slices were detached from the glass with nitromethane and mounted on adhesive tape for the beamline experiments. Raman analyses were performed on polished thin sections, since the irregular surface of the beamline specimens on tape interfered with the spectroscopic signal. Petrographic studies of polished thin sections used an Olympus BX53M microscope in the Bowen Laboratory, Department

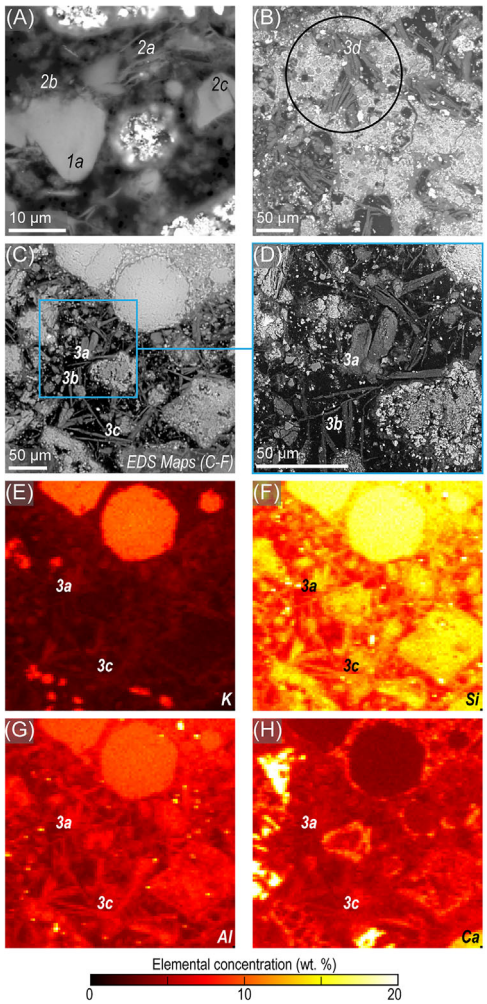

FIGURE 4 SEM-BSE and EDS images of C-A-S-H microstructures in the 06-CMETELLA-C1 mortar sample. (A) Higher magnification image of the area of μXRD analyses showing incipient elongate features (*site 2c*, see also Figure 3), incipient splitting of C-A-S-H domains (*sites 2a, 2b*), and apparent dissolution and production of wispy features around C-A-S-H domains. (B) Pronounced splitting of C-A-S-H domains into elongate features occurs in the interfacial zone and vesicles (*site 3d*) of a large scoria. (C, D) Overview of the diverse features of the binding phase showing partially intact C-A-S-H domains (*sites 3a, 3b*) and elongate features (*site 3c*). (E–H) Quantified EDS maps (wt %) of K, Ca, Al, and Si, respectively, in the cementing matrix

of Geology and Geophysics, University of Utah (Figures 2 and 8).

2.2 | X-ray microdiffraction

Experiments at Advanced Light Source Beamline 12.3.2 investigated submicron-sized phases with microdiffraction using a monochromatic X-ray beam (Figure 2).[26,27] The mortar slice mounted on tape was loaded in transmission mode, with the detector placed at 39° to the incident beam. A monochromatic X-ray beam of 10 keV was focused to 2 × 5 μm spot size. A DECTRIS Pilatus 1M area detector placed at about 150 mm recorded Debye rings from crystalline phases. The experimental geometry was calibrated using α-Al_2O_3 powder. X-ray diffractograms were produced with *d*-spacing reflections integrated radially for 2θ 4–54° over a 40° arch segment (χ) around the cone of diffraction. These are shown as Debye diffraction plots (Figures 2 and 3B, C, E) and intensity versus d-spacing plots (Figure 3D). For high precision powder X-ray diffraction analysis of the 06-METELLA-C2 sample, see reference 21. Data were processed using the XMAS software.[28]

2.3 | Raman spectroscopy

Raman spectroscopy was performed with a WiTec Alpha 300 R confocal Raman microscope (Figures 5–8). Samples were imaged using a Zeiss Epiplan-Neofluar 100 × objective lens (NA 0.9). Samples were excited with a Research Electro-Optics 35 mW helium-neon 633 nm laser at 1/3 power. Two accumulations of 45 s each were averaged at each point in the scan and a 600 g/mm spectrometer grating was used. Lateral resolution for area scans varied from 4 to 5 μm. Data were processed using the WiTec Project 5 software. After background removal, the signal from the embedding medium was subtracted from each scan. The software's built in k-means clustering function was used to identify component spectra of each scan. Maps indicating the intensity of each component at all points in the scan were then generated. For the peak broadening analysis of the leucite distribution, a central difference second derivative approximation was used to determine the position of the three composite peaks. These positions were used as the location for the fitted Gaussian curves in the WiTec Project 5 software. Full width at half maximum values were plotted using MATLAB R2020a.

2.4 | SEM and EDS

The SEM-EDS data in Figures 4C–H, 5, and 7 were acquired on a Tescan Vega 3 XMU scanning electron microscope in variable pressure mode (20 Pa, gas: N_2, accelerating voltage: 20 keV). EDS maps were acquired with a Bruker XFlash 630 silicon drift detector with sufficient acquisition time to achieve at least 2000 counts per pixel in the mapped area to detect elements ≥1 wt%. To compare compositions of the C-A-S-H structures in Figure 4, five point analyses were carried out on each structure type using the "exhaustive" setting (10^6 total counts per spectrum) to achieve an error ≤ 0.15 wt% in

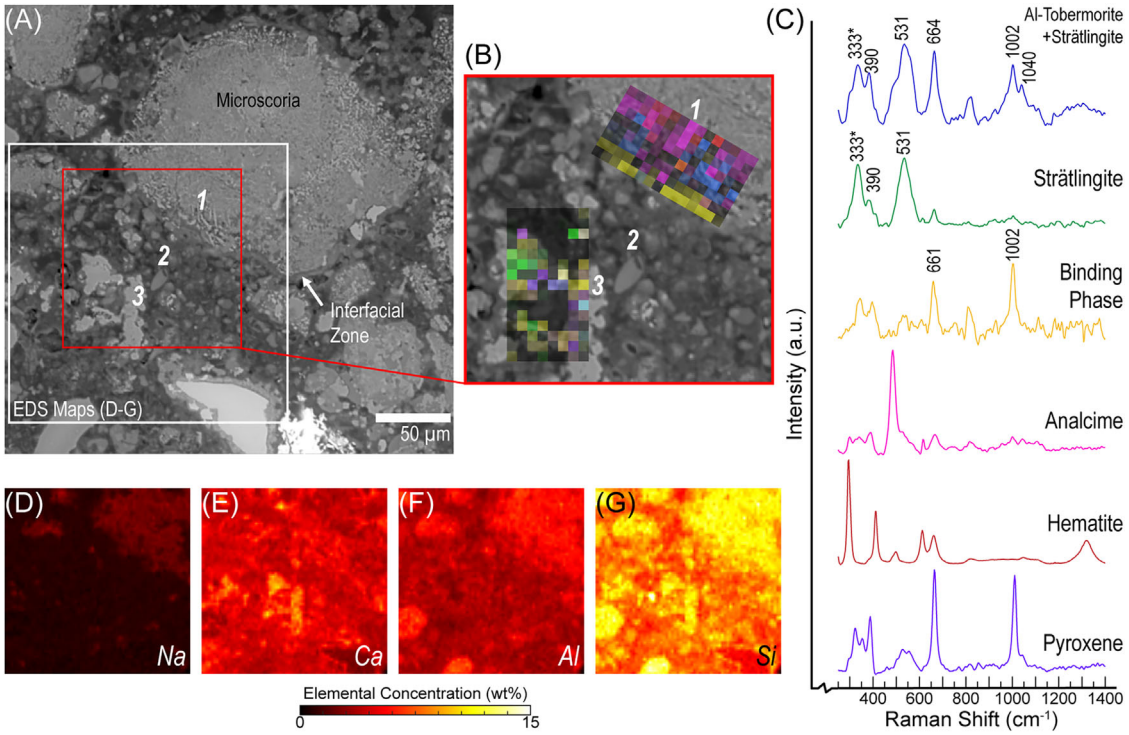

FIGURE 5 Correlative Raman and SEM-EDS spectroscopic analyses describe the interface of a Pozzolane Rosse microscoria and the surrounding cementing matrix (see also Figure 1D–F), 06-CMETELLA-C2 sample. (A) SEM-BSE micrograph showing the interfacial zone (*site 1*), the binding phase (*site 2*), and a partially altered clinopyroxene crystal (*site 3*). (B) Raman imaging (overlain on the SEM-BSE micrograph) shows the distribution of crystals in the tephra (pyroxene, hematite, and analcime) and cementing phases present in the interfacial zone (the C-A-S-H binding phase, strätlingite and (Al)-tobermorite). (C) Color-coded Raman spectra corresponding to the components identified in (B). (D–G) Elemental distributions showing the wt. % concentrations of Na, Ca, Al, and Si, respectively. Mineral assignments from RRUFF (see also Figure 5)[34]

quantification of Al, Si, K, and Ca. EDS data were quantified using the Bruker Esprit 2.1 Software with PB Linemarker-ZAF correction.

The SEM back-scattered-electron (BSE) images of Figures 1 and 4A, B were acquired using the JEOL IT3000 at the Energy & Geoscience Institute (EGI) at the University of Utah using uncoated thin sections with an accelerating voltage of 25 kV, a beam (probe) current of 65 nA, and low vacuum at 100 Pa. The primary detector used for imaging was a compositional BSE detector. The SEM EDS images of Figure 3 were acquired with a Zeiss EVOMA10 Scanning Electron Microscope at the Department of Earth and Planetary Science at UC Berkeley.

3 | RESULTS

The mortar of the Tomb of Caecilia Metella concrete is composed of granular particles of Pozzolane Rosse tephra that are bound together by a complex cementing matrix, consisting of a binding phase and fine sand-sized volcanic ash (Figure 1D). (Volcanic ash refers to the <2 mm fraction of a tephra deposit.) The coarser fraction of tephra can be considered as aggregate, yet it has the same composition as the fine ash of the cementing matrix. Both are composed of scoriae (and microscoriae <0.1 mm) with a groundmass high in potassium (4–5 wt% K_2O) and low in silica (45–46 wt% SiO_2) and primary volcanic crystals of clinopyroxene, leucite, and magnetite. Authigenic components, produced by alteration over tens of thousands of years within the pyroclastic flow deposit, include analcime replacing leucite, as well as opal and halloysite clay mineral coatings.[10] Petrographic micrographs demonstrate that the perimeters of most clinopyroxene and leucite crystal fragments, regardless of size, have a dissolution and/or alteration rim at the interface with the cementing matrix (Figure 1D, upper left of image). These could be interpreted as relicts of pozzolanic processes. However, the perimeters of leucite crystals, in particular, show serrated edges that grade into the extant cementing matrix (Figure 1D) or distinct dissolution microstructures (Figure 7), suggesting processes which postdate the early pozzolanic reactions that produced the C-A-S-H binder.

The C-A-S-H of the binding phase shows three principal features: (1) discrete domains of mainly intact C-A-S-H approximately 20–50 μm in size (Figure 2, see also

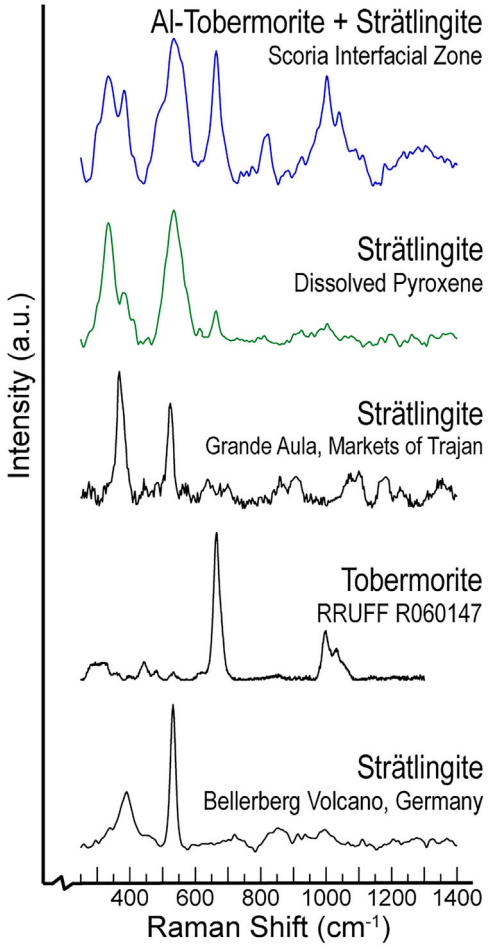

FIGURE 6 Raman spectra of Al-tobermorite and strätlingite from the interfacial zones of Pozzolane Rosse scoriae and clinopyroxene (Figure 4A–C) are compared to ideal tobermorite,[34] strätlingite in the wall mortar of the Grande Aula concrete, Markets of Trajan and strätlingite from Bellerberg volcanic deposits, Germany

Figure 1F *site 2*, Figure 3A *sites 1a, 1a'*, and Figure 4A *sites 1a, 1a'*), (2) etching or dissolution that occurs around the perimeter of a discrete C-A-S-H domain, which may be accompanied by a halo of thin, fine, wispy features or by tendril-like strands that protrude from the dissolving C-A-S-H (Figure 1F *site 2'*, Figure 3A *sites 2a, 2b*, and Figure 4A *sites 2a, b*), and (3) elongate features that appear to develop by splitting of the C-A-S-H domains (Figure 4B–D *sites 3a, 3b, 3c, 3d*). Note that some C-A-S-H domains show faint linear traces and incipient splitting (Figure 3A *site 2c* and Figure 4A *site 2c*). In some instances, clinopyroxene crystals have developed alteration rinds, from which fine wispy halos protrude (Figure 1F *site 3*). Furthermore, leucite crystals show pronounced etching and dissolution (Figures 1D and 7). Together, the microstructures in the C-A-S-H binding phase, the alteration rinds of clinopyroxene crystals, and the dissolution of leucite crystals suggest pervasive processes of dissolution and reorganization in the mortar that have not been identified in previous studies of late Republican and Imperial era architectural concretes in Rome.[11,20,29,30] The analytical descriptions of microstructures in Figures 2–7 provide insights into these diverse processes.

3.1 | Cementing matrix μXRD and SEM-EDS

The SEM image of Figure 3A shows a typical example of the Pozzolane Rosse microscoriae and binding phase that form the cementing matrix of the mortar. The grid of μXRD analyses is overlain on the SEM image (Figure 3A, E); it includes a microscoria, its interfacial zone, and the neighboring binding phase. A Debye diffraction plot shows that clinopyroxene, magnetite, and hematite are the principal crystals in the microscoria; fine-grained analcime and calcite are also present (Figure 3B). This is a typical mineral assemblage of the least altered facies of Pozzolane Rosse, where very fine leucite crystals are replaced by analcime but larger leucite crystals (Figure 7) remain mainly intact; the volcanic glass is slightly altered.[10] C-A-S-H binder occurs as partially intact domains (Figure 3A *sites 1a, 1a'*, for example) where μXRD analysis (Figure 2) shows broad expressions of typical 5.4 and 3.0 Å d-spacings.[31–33] Note that the Debye rings are broadly diffuse around the cone of diffraction, indicating a nanocrystalline structure with no preferred orientation. The X-ray beam also detects d-spacings from analcime, hematite, magnetite, and clinopyroxene in the neighboring microscoria.

At the interface with the larger microscoria, however, the C-A-S-H has apparently undergone pervasive in situ alteration (Figure 3A *sites 2a, 2b*). The C-A-S-H domains have diffuse perimeters partially surrounded by wispy features, or halos; long, narrow strands, or tendrils, approximately 10 μm in length, protrude into the cementing matrix. The μXRD analysis of the tendril-like strands reveals a broad Debye diffraction ring with the highest intensity centered at approximately 5.4 Å, which extends gradually to 3.6 and 6.5 Å (Figure 3C, E *site #019*). This pattern indicates a nanocrystalline phase that also has a preferred orientation between −62° and 62° χ; there is no apparent 12 Å reflection.[31–33] The broad expression of this diffraction pattern as compared to the crystalline components of the tephra (Figure 3D) further describes these nanocrystalline characteristics. The *d*-spacings of the broad reflections correlate with 2.98–3.00 Å and 5.37–5.45 Å reflections in powdered C-A-S-H produced through laboratory syntheses[31] as well as other C-A-S-H syntheses.[33] The integrated intensity of the broad 5 Å reflection of

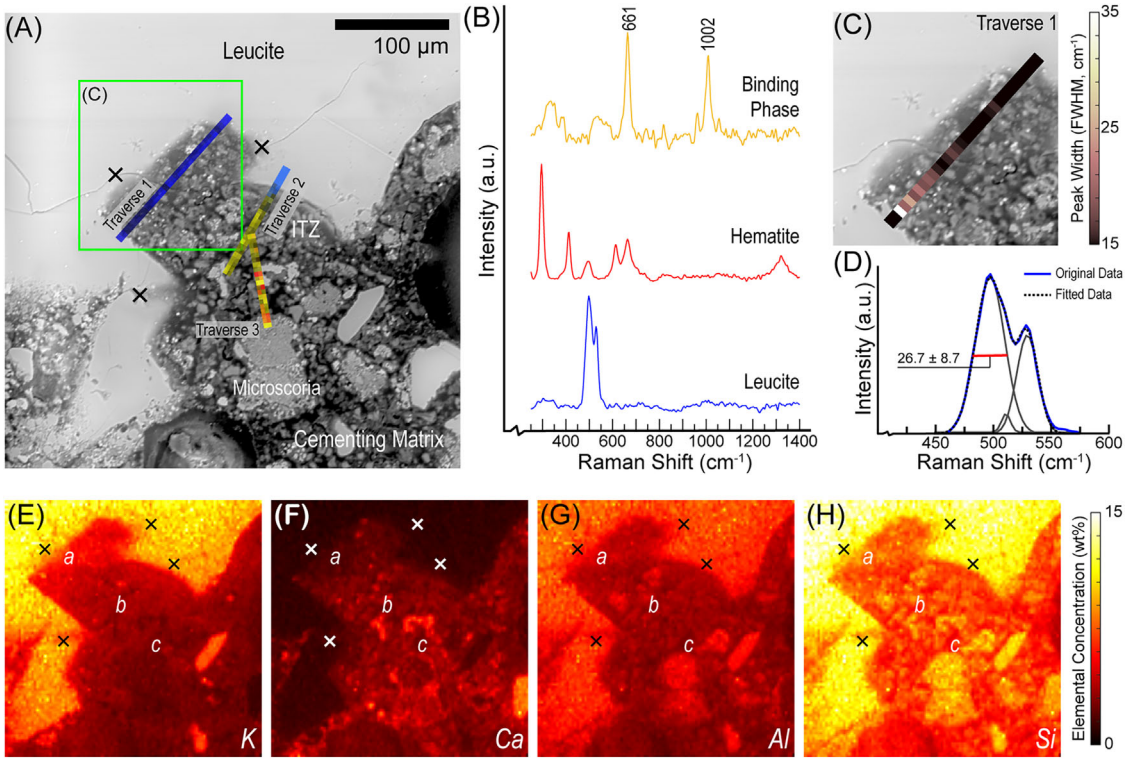

FIGURE 7 Correlative Raman and SEM-EDS spectroscopic analyses reveal a gradient of dissolution in the interfacial zone of a Pozzolane Rosse leucite crystal fragment 06-CMETELLA_C2 mortar sample. (A) SEM-BSE micrograph of the leucite, interfacial zone, and cementing matrix with overlays showing the distribution of phases identified via Raman imaging along traverses 1–3. The sites marked "x" indicate traces of relict microcracks in the crystal as well as compositional gradients in the EDS maps. (B) Color-coded spectra of components corresponding to traverses in (A). (C) Progressive dissolution of leucite in the interfacial zone is identified through a broadening of the 495 cm^{-1} SiO_4 bending band. (D) Schematic of the full width at half maximum (FWHM) calculation plotted in traverse 1 (A, C). (E–H) Elemental distributions showing the weight percent concentration of K, Ca, Al, and Si, respectively. Mineral assignments from RRUFF[34]

the C-A-S-H (Figure 3E) indicates that the signal is strongest close the interface with the scoria, correlating to the tendril-like strands identified through SEM imaging (Figure 3A). By contrast, the partially intact C-A-S-H domains with incipient traces of opening separation show no nanocrystalline structure or preferred orientation (e.g., Figure 3A, E *site 1b*).

SEM images show that the more intact C-A-S-H domains (Figure 3A, *site 1a*, Figure 4A *site 1a*, and Figure 4C, D *site 3a*) occur throughout the cementing matrix of both the facing of the concrete wall (06-CMETELLA-C1) and the crest of the barrel vault (06-CMETELLA-C2). However, the elongate features that appear to develop by splitting of the C-A-S-H domains (Figure 4B–D *sites 3b, 3c, 3d*) more commonly occur in the 06-CMETELLA-C1 sample, the facing of the concrete wall. Furthermore, they are most pronounced near scoriae (Figure 4C *site 3c* and D *site 3b*) or within vesicles of scoriae (Figure 4B *site 3d*). Notably, the EDS data (Figure 4E–H) reveal a slightly higher concentration of K (Figure 4E) and Si (Figure 4F) in the partially intact C-A-S-H structures (3.8 wt% K and 12.6 wt% Si, Figure 4E, F *site 3a*) compared to the elongate features (2.5 wt% K and 10.3 wt% Si, Figure 4E, F *site 3c*). Ca and Al concentrations (Figure 4G, H), however, are similar (5.6 wt% Ca, 6.6 wt% Al in intact structures, 5.1 wt% Ca, 6.1 wt% Al in elongate features). These values indicate exceptionally low values for Ca/(Si+Al), giving 0.29 for the partially intact C-A-S-H domains and 0.31 for the elongate features. They also indicate a small but non-negligible amount of potassium released to the mortar system through the splitting process. By contrast, the Markets of Trajan mortar reproduction at 180 days hydration has C-A-S-H domains with Ca/(Si+Al) ≈ 0.8–0.9.[20] The contiguous C-A-S-H domains in the ancient Markets of Trajan mortar have Ca/(Si+Al) ≈ 0.45–0.75 and Na_2O+K_2O ≈ 1.5 at%. There is thus substantially greater incorporation of Al^{3+} and K^+ in the mainly intact C-A-S-H domains of the Caecilia Metella mortar samples, suggesting that different post-pozzolanic processes have occurred in this concrete.

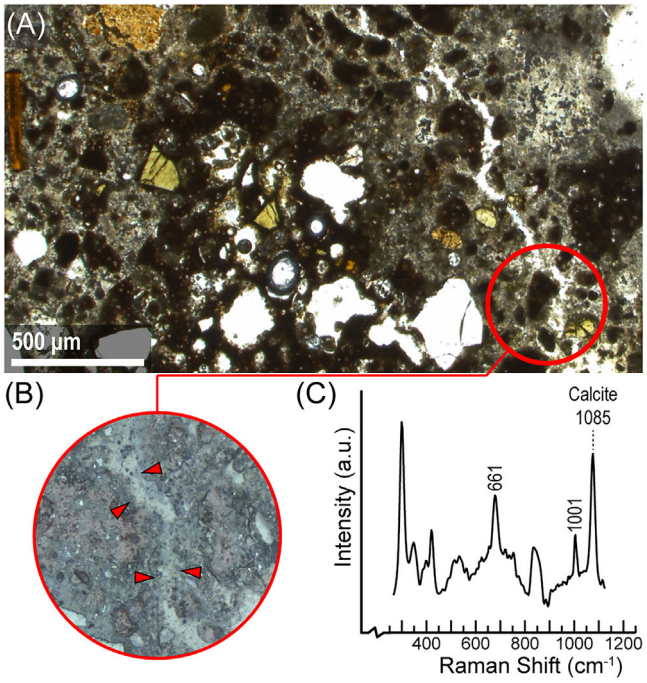

FIGURE 8 Microcrack in the 06-CMETELLA-C1 mortar sample. (A) Petrographic image (PPL) shows the microcrack traversing the cementing matrix. (B) Reflected light confocal micrograph of an infilled area from (A) indicating the points at which Raman spectra were acquired. (C) Average Raman spectrum revealing calcite as the primary component within the microcrack walls

3.2 | Microscoria interface with the cementing matrix

A narrow zone of acicular features occupies the interface of a Pozzolane Rosse microscoria with the cementing matrix (Figure 1D–F *site 1* and Figure 5A *site 1*). This zone and the adjacent cementing matrix, including a clinopyroxene crystal (Figure 1D–F *site 3* and Figure 5A *site 3*) with an intact interior but a pronounced rind of dissolution and alteration along its perimeter (Figure 4A *site 4*), are investigated using correlative Raman spectroscopy and SEM-EDS imaging and analysis to gain insights into variations in chemical and mineralogical characteristics at the micrometer scale. These variations are shown by two grids of Raman analyses that are color coded to phase identifications (Figure 5B, C). SEM-EDS analyses show corresponding variations in Na, Ca, Al, and Si (Figure 5D–G). In the interfacial zone of the microscoria (Figure 5B *site 1*), the composite Raman spectrum of the acicular features corresponds to spectra from tobermorite[34] and strätlingite crystals (Figure 6). The reference spectra for strätlingite were acquired using the same acquisition parameters on known strätlingite crystals in the mortar of the Grande Aula wall concrete in the Markets of Trajan (see reference 20 for further information) and metamorphosed limestone xenoliths from Bellerberg volcano, Germany. The strätlingite spectrum also occurs at the perimeter of the clinopyroxene crystal (Figure 5A, B *site 3*, see also Figure 1 *site 3*).

By contrast, the adjacent binding phase (Figure 5A, B *site 2*) has Raman peaks at 661 cm^{-1} (SiO_4 bending) and 1002 cm^{-1} (SiO_4 stretching), consistent with laboratory synthesized C-A-S-H.[35] Note, however, that this spectrum has similarities to that of certain clinopyroxene crystals.[34] The Raman spectrum of the intact interior of the clinopyroxene in the nearby cementing matrix (Figure 1F *site 3* and Figure 5A *site 3*) is consistent with augite,[34] with the SiO_4 bending band at 667 cm^{-1} and the SiO_4 stretching band at 1010 cm^{-1} (Figure 5C). Conversely, the binding phase spectrum has Raman peaks of 661 cm^{-1} for the bending band and 1002 cm^{-1} for the stretching band (Figure 5C); these peaks are systematically correlated with C-A-S-H domains at the interfacial zones of Pozzolane Rosse scoriae and microscoriae throughout the cementing matrix (e.g., Figures 6 and 7). The Raman scan and spectra of Figure 5B, C *site 3* thus verify that the binding phase spectrum and the clinopyroxene spectrum can be distinguished by the positions of the dominate SiO_4 bending and stretching bands.

Quantified EDS elemental mapping (as wt%) of the scoria and cementing matrix (Figure 5D–G) indicates high calcium concentration in the clinopyroxene crystal and calcium enrichment in the binding phase and scoria interface (Figure 5E). The calcium content then decreases toward the interior of the scoria, with the groundmass and volcanic crystals having higher Na, Al, and Si concentrations. The acicular phases in the interfacial zone have a relatively high concentration of aluminum (Figure 5F), suggesting that Al-tobermorite ($[Ca_4(Si_{5.5}Al_{0.5}O_{17}H_2)]Ca_{0.2}{\cdot}Na_{0.1}{\cdot}4H_2O$)[36,37] rather than ideal tobermorite ($Ca_5Si_6H_2O_{18}{\cdot}4H_2O$)[33,36] occurs with strätlingite in the scoria interface. C-A-S-H binder has been previously shown to be the product of pozzolanic reaction with hydrated lime and Pozzolane Rosse tephra[20] and, as such, calcium is expected to be elevated in interface. The elevated Si and Al in the interfacial zone relative to that of the binding phase suggests, however, that long-term, post-pozzolanic chemical interactions at the microscoria perimeter may have produced the crystalline phases.

3.3 | Leucite crystal interface with the cementing matrix

A leucite crystal fragment with an intact interior and complex zone of dissolution at its perimeter provides an instructive reference for evaluating in situ changes at the crystal interface with the cementing matrix (Figure 7).

Three traverses mapped with Raman micro-spectroscopy describe this interfacial zone (Figure 7A); the component spectra are identified in Figure 7B. The leucite spectrum (blue) is most distinct in traverses 1 and 2 (Figure 7A). In traverse 2, the Raman signal for leucite, shown in light blue, stops abruptly at the edge of the intact crystal fragment; the spectra of the binding phase (yellow) are detected in the adjacent cementing matrix (Figure 7A, B). By contrast, in traverse 1, the Raman signal for leucite varies in intensity from lighter blue to darker blue (Figure 7A, B).

The variations in the SiO_4 bending region of the leucite spectrum of traverse 1, enlarged in Figure 7C, were examined by peak fitting with three Gaussian curves at 497, 510, and 530 cm^{-1} (Figure 7D). The peak fitting reveals a broadening of the component peaks from the upper right to the lower left sectors of traverse 1, and most notably in the peak corresponding to 497 cm^{-1} (Figure 7C, D). In the intact crystal, this peak has a width (FWHM) of 16 cm^{-1} yet it broadens to up to 35 cm^{-1} in the lower interface with the cementing matrix. Such broadening indicates a more disordered configuration, consistent with progressive dissolution of the leucite perimeter.

Note that the original perimeter of the leucite crystal appears to have originally extended to the upper sector of traverse 3 and is recorded by traces of relict microcracks in the crystal (Figure 6A *sites of crack traces marked "x"*) as well as gradients in the EDS maps (Figure 6E–H). The gradual decrease in potassium concentration extends from the current crystal perimeter above traverse 1 (Figure 6E, *site a*) through the transitional dissolution zone at the original crystal perimeter within traverse 3 (Figure 6E, *site b*) to the potassium-enriched cementing matrix adjacent to the crystal (Figure 6E, *site c*). The SEM image (Figure 6A) reveals pervasive dissolution halos surrounding 10–15 μm domains of C-A-S-H in this zone; the cementing matrix from *site a* to *site b* originally formed the interfacial zone underlying the intact crystal. The hematite of traverse 3 represents traces of the ground mass of Pozzolane Rosse microscoriae in the cementing matrix. Raman maps at 5 μm grid spacing along traverses 2 and 3 (Figure 6A) indicate that the intensity of the binding phase spectrum increases next to microscoriae and the hematite spectra.

4 | DISCUSSION

The integrated results of microdiffraction and spectroscopic analyses indicate that profound transformations in the C-A-S-H binding phase, as well as the diverse components of Pozzolane Rosse tephra aggregate, have substantially remodeled the cementing matrix and interfacial zones of the Tomb of Caecilia Metella mortar over the past 2050 years.

4.1 | C-A-S-H microstructures

4.1.1 | C-A-S-H morphologies

C-A-S-H binder in the mortars of the late Republican era Theater of Marcellus and Imperial era Markets of Trajan concretes occurs as a rather uniform, contiguous phase that extends over tens of microns.[11,20] Nanocrystalline reflections in μXRD studies of C-A-S-H in the cementing matrix of the Markets of Trajan mortars have not been previously described. However, strätlingite crystals up to 30 μm in length are common in the interfacial zones of the ancient mortar and its reproduction at 180 days hydration.[20] By contrast, μXRD analyses of the Tomb of Caecilia Metella cementing matrix reveal a general absence of strätlingite (Figures 2 and 3). Furthermore, intact domains of C-A-S-H and incipient elongate features do not show nanocrystalline reflections. However, μXRD analyses of wispy halos and tendril-like strands around intact domains of C-A-S-H reveal a dominant broad reflection that is centered at approximately 5 Å *d*-spacing and extends to 3.6 and 6.5 Å; there is another broad reflection at 3.0 Å (Figures 2 and 3). Reflections at 3.0 and 5.4 Å have been previously identified in studies of experimental syntheses of C-A-S-H.[31–33] The C-A-S-H that occurs as tendril-like strands is further characterized by significantly broader reflections expressed from –62° to 62° χ, instead of the full range of the Debye diffraction ring. This indicates a preferred orientation in the nanocrystalline structure of the tendril-like features (Figure 3E).

The broad reflections in the μXRD analyses of the binding phase (Figure 3C, D) overlap with several sharp reflections produced by clinopyroxene within the tephra aggregate at 2.9, 3.0, and 4.7 Å (Figure 3D). Further, the Raman spectrum identified with the binding phase (Figures 5C and 7B) is similar to that of clinopyroxene; both have chain-silicate structures. The SiO_4 bending and stretching peaks associated with the binding phase, however, are shifted toward lower wavenumbers, 661 cm^{-1} for the bending band and 1002 cm^{-1} for the stretching band (Figure 5C). These data suggest that, overall, the C-A-S-H binding phase does have short range order as a layered chain silicate. However, the lower Raman shifts and broad μXRD reflections indicate that the long-range order is disrupted. This is consistent with laboratory syntheses of C-(A)-S-H, albeit with higher calcium contents, which tend toward a collection of finite silica chain lengths[39,40] and subsequently exhibit lower wavenumber Raman shifts of SiO_4 vibrations. It is possible that potassic ions disrupt the long-range order of the binding phase, as described in alkali-rich laboratory syntheses of C-(A)-S-H.[32,41] The spectral resolution (4 cm^{-1}) for the Raman spectroscopic data presented here is insufficient, however, to distinguish subtle differences in the spectra associated with varying potassium contents.

The Raman spectrum of the binding phase is also consistent with peaks observed for C-A-S-H in the mortar of the *Baianus Sinus* breakwater marine concrete (443, 670, and 994 cm^{-1}) after signal from the embedding medium is removed.[22] The absence of calcite in the Raman signal (distinguishable by a strong carbonate υ_1 vibration at ~1085 cm^{-1}) in the Tomb of Caecilia Metella binding phase and the paucity of calcite and vaterite in the μXRD analyses indicate that little carbonation has occurred. Interestingly, the calcium content of the binding phase is extremely low (Ca/(Si+Al) = 0.29–0.31), even when compared to the Markets of Trajan binding phase (Ca/(Si+Al) = 0.45–0.75).[20]

4.1.2 | Post-pozzolanic processes

The elevated potassium in intact C-A-S-H domains (Figure 4E) suggests that complex post-pozzolanic processes occurred after the consumption of $Ca(OH)_2$ was complete. At 2050 years hydration, Ca/(Si+Al) is now 0.29 in the intact C-A-S-H domains and 0.31 in the elongate C-A-S-H features; K decreased from 3.8 wt% in the intact domains to 2.5 wt% in the elongate features. This represents a substantial reduction in the initial Ca/Si ratio of the C-A-S-H at 6 months hydration, which has been shown to be in the range of Ca/(Si+Al) ≈ 0.8–0.9.[20] In comparison, the contiguous C-A-S-H domains in the ancient Markets of Trajan mortar have Ca/(Si+Al) ≈ 0.45–0.75 and Na_2O+K_2O ≈ 1.5 at%.

Binding of alkali in C-A-S-H has been thought to occur through a valence compensation mechanism, so that the potential charge imbalance created by substitution of Al into tetrahedral sites for Si is balanced by inclusion of alkali, $M^+ + Al^{3+} = Si^{4+}$; Al has a progressively greater influence on alkali sorption in low Ca/Si gels.[42] Recent studies of C-(N,K-)A-S-H composition, structure, and solubility relationships indicate that alkali uptake is most strongly increased in the presence of solutions with low calcium or high alkali hydroxide concentrations, up to 0.5 mol/L KOH for Al/Si ≤ 0.1.[31,32,41] Alkali sorption rearranges the C-A-S-H structure so that less calcium is present in the interlayer; meanwhile, high sodium and potassium uptake in the interlayer decreases the interlayer distance, shortens silica chain length, and may increase the cross-linking of silicate chains.[31,32] A recent atomistic and mesoscopic assessment of alkali uptake in cement paste investigates Na and K adsorption at the pore surface of calcium silicate hydrates (C-S-H) as well as the hydrated interlayer.[43] The modeling suggests that Na and K adsorption produces a small reduction in the elastic modulus and volume expansion in C-S-H grains.

In the context of these recent investigations, the wispy halos that occupy pore surfaces surrounding etched C-A-S-H domains in the Tomb of Caecila Metella mortars (Figures 3A, 4A, 5A, and 7A) suggest surface dissolution and the creation of new, post-pozzolanic, C-(K)-A-S-H nanocrystalline fabrics (Figure 3). Indeed, nanocrystalline fabrics have been previously described in highly polymerized C-S-H with "semi-crystalline" XRD reflections produced from blast furnace slag activated with KOH.[44] The wispy halos seem to create zones of greater internal cohesion within the binding phase at the 5–50 μm scale (Figures 5A and 7A); the apparent progression to tendril-like strands may present obstacles to propagation of microcracks (Figures 3A and 4A).

By contrast, the C-A-S-H domains that split into elongate features (Figure 4B–D) suggest processes of interlayer alkali adsorption that rearrange and remodel the pozzolanic C-A-S-H fabric. When a hydrous alkali aluminosilicate gel such as C-A-S-H ages, the chemical environment in the pore solutions to which the binder is exposed may also evolve.[31,32,45] The alkali sorption experiments of Hong and Glasser[42] illustrate, for example, an increase in alkali concentration in the aqueous phase when C-A-S-H desorbs sodium; compositional tie-lines exist between the coexisting solid and pore solution. In the Tomb of Caecilia Metella mortars, the initial pozzolanic Ca/Si ratio in C-A-S-H domains, about 1.15, decreased to 0.44 in intact domains-and then increased to 0.50 in the elongate features. It is not entirely clear how the potassium concentrations in the C-A-S-H record long-term alkali solution–gel interactions with the highly potassic groundmass and leucite crystals of the Pozzolane Rosse aggregate or the eventual splitting mechanisms of the intact C-A-S-H domains. It is possible that potassium enrichment to 3.8% in the intact domains (Figure 4) may have caused mechanical destabilization of the layered C-(K-)A-S-H and irreversible volume expansion through adsorption of the large potassium cations. The highly porous nature of the cementing matrix would have mitigated these expansive processes.[46] Alternatively, if the pore solution chemistry changed abruptly through, for example, an influx of rainwater or groundwater, the C-(K)-A-S-H could have released potassium ions from the interlayer into the pore fluid, splitting the intact domains along interlayer sites suddenly devoid of alkali cations.

4.2 | Interfacial Al-tobermorite and strätlingite

Raman spectra indicate the presence of strätlingite and Al-tobermorite with acicular morphologies associated with the interfacial zone of a Pozzolane Rosse microscoria (Figure 5A–C *site 1*). Strätlingite also occurs in the interfacial zone of a dissolving clinopyroxene (Figure 5B *site 3*). The Raman peaks corresponding to the strätlingite do

exhibit some broadening compared to strätlingite from Bellerberg volcano and the mortar of the Grande Aula wall concrete (Figure 6). This is perhaps due to the presence of katoite, a hydrogarnet, and cementing mineral in Markets of Trajan mortars,[20] which has broad peaks at ~500 and ~540 cm^{-1}.[47] Experimental reproduction of the Markets of Trajan mortar showed that strätlingite began to crystallize at ≤90 days hydration, after portlandite ($Ca(OH)_2$) was fully consumed through pozzolanic reaction processes.[20] The platey crystals then began to toughen interfacial zones along scoria perimeters and impede the macroscale propagation of microcrack segments. These microstructures, consisting mainly of interfacial strätlingite and coalesced domains of C-A-S-H binder, are pervasive in the architectural mortars of the Markets of Trajan and the Theater of Marcellus.[11,20] The Ca/Si ratios in intact C-A-S-H domains of the Markets of Trajan mortars have remained relatively stable, from about 1.15 at 6 months hydration to 1.12 at 2050 years hydration.[20]

Strätlingite is far less common in the 06-METELLA-C1 and 06-METELLA-C2 mortar samples of Tomb of Caecilia Metella concrete. It is confined to intermittent localities along the perimeter of tephra particles and has not been detected in the cementing matrix. The original pozzolanic interfacial zone and binding phase have evidently undergone progressive evolution at ambient temperatures, high relative humidity, and ground and surface water penetration; this evolution has led to localized toughening of some interfacial zones.

4.3 | Leucite dissolution into cementing matrix

Progressive dissolution of the perimeter of a leucite crystal is associated with broadening of Raman bands and steep gradients in elemental compositions that persist through 25–100 μm of the neighboring cementing matrix (Figure 7). A narrow potassic rind, 10–50 μm in thickness, with some depletion of Al and Si, occurs at the edge of the more-or-less intact crystal (Figure 7E–H) but there is no evidence for expansive behavior or microcracks that would be associated with alkali-silica-reaction in OPC concretes. There is, however, an elevated EDS spectroscopic signal for potassium in the broad leucite interfacial zone compared with the more distant cementing matrix (Figure 7E). Where potassium concentrations are elevated (Figure 4E *site 3*), C-A-S-H domains have halos of linear and wispy features that suggest pervasive in situ dissolution and reconfiguration of the pozzolanic binding phase, whereas in the more distant cementing matrix, the C-A-S-H domains appear somewhat more intact. The intensity of the Raman spectra of the binding phase is strong in immediate contact with microscoriae (Figure 7A *traverse 3*) where intact C-A-S-H domains are, perhaps, more prevalent. It is possible that elevated potassium elsewhere in the leucite dissolution zone has contributed to destabilization of the C-A-S-H domains and a decrease in the intensity of the Raman spectra of the binding phase.

4.4 | Insights into chemical and mechanical resilience

The interface between aggregates and cementing binder is of primary interest for concrete durability studies. The interfacial transition zone in OPC mortar and concrete is susceptible to a variety of degradation pathways, including mechanical failure[48–50] and alkali-aggregate reaction (AAR).[51] Aggregates are, therefore, selected to be inert, with very low contents of amorphous silica and alkali, $Na_2O + K_2O \leq 0.6$ wt%,[52] to reduce expansive and deleterious reactions. However, the inert aggregate consequently has a porous interfacial transition zone with the cement paste that is prone to interfacial crack propagation.[53] The addition of supplementary cementitious materials, such as silica fume, fly ash, and slag, to OPC concrete has been shown to densify the interfacial transition zone by consuming excess portlandite that disrupts the packing of cementing phases.[54–56] Such densification is expected to lower permeability and improve the mechanical performance of the concrete, thus reducing degradation effects.

Post-pozzolanic processes, or the evolution of the mortar after portlandite ($Ca(OH)_2$) has been fully consumed, have been linked to durability in both ancient Roman architectural[20] and marine[22] constructions. In the reproduction of the Markets of Trajan mortar, strätlingite crystallizes at the interface of volcanic aggregate particles only after portlandite has been fully consumed through pozzolanic reactions and production of C-A-S-H binder.[20] Further, the incompatibility of portlandite and strätlingite has been well-described.[19,57] In Roman marine concretes, in situ dissolution of tephra components has also produced post-pozzolanic mineral cements, principally Al-tobermorite and phillipsite but also strätlingite in the case of sanidine dissolution.[22] In the Tomb of Caecilia Metella mortars, strätlingite and Al-tobermorite mineral cements occur intermittently at the perimeter of scoriae and clinopyroxene crystals (Figures 4 and 5), suggesting discontinuous toughening of the interfacial zones of these aggregate components.

The paucity of calcite and vaterite in intact regions of the binding phase in the Caecilia Metella mortar suggests that (1) pozzolanic reaction processes went to completion so that no portlandite remained to carbonate and (2) subsequent carbonation of the binding phase is very

limited. When the post-pozzolanic dissolution of silicate components of the tephra aggregate occurred, alkali-rich gel formation was not favored, possibly due to insufficient calcium availability. This is in stark contrast to OPC mortars and concretes, in which portlandite is a by-product of hydration and critical to maintaining the passivation of steel reinforcement. Portlandite is nearly always available to progress to AAR. It is possible that some aged blended cement concretes could approach a post-pozzolanic state though, in one example, portlandite is still detected in a fly ash and slag cement paste after 20 years hydration.[51,58] However, Al-tobermorite has crystallized in the thick OPC concrete walls of a decommissioned nuclear power plant in Japan in the absence of portlandite at 40–55°C and 16.5 years hydration, greatly increasing the strength of the concrete.[59]

In the two Tomb of Caecilia Metella mortar samples investigated here, post-pozzolanic crystalline mineral cements are not readily detected in the binding phase. It is apparent, however, that intact C-A-S-H domains (Figures 2 and 3A *site 1a*, 4a *site 1a*) have evolved to produce wispy halos and tendril-like strands of C-A-S-H with a nanocrystalline preferred orientation (Figure 3C) or, alternatively, elongate features that divide previously intact domains (Figure 4B *site 3d*, and 4C, D *sites 3b, 3c*). These elongate features are ubiquitous in the cementing matrix of the 06-METELLA-C1 mortar; they remain an enigma worthy of further study.

It is not possible to derive a quantitative measure of the coherence of the cementing matrix from the very small archaeological samples of the mortars. At the macroscopic scale, however, the brick facing and mortar joints of the sepulchral corridor are highly compact (Figure 1C); bricks have not detached from the corridor walls and there is little or no disaggregation of mortar particles from the corridor walls or the conglomeratic concrete of the barrel vault. These features indicate a highly robust concrete system that has maintained cohesion to an exceedingly high degree over two millennia.

It may be that the reorganization of the C-A-S-H domains into wispy and elongate features provides obstacles to microcrack propagation in the cementing matrix of the mortars. A microcrack identified through petrographic analysis reveals regions of infill between the crack walls (Figure 8A). Raman spectroscopy analysis at four points (Figure 8B) describes the infill. The four spectra, averaged to reduce noise, reveal peaks corresponding to the cementing binding phase (661 and 1001 cm^{-1}). These have moderate intensity, while a carbonate peak corresponding to calcite (1085 cm^{-1}, CO_3 stretching) has strong intensity. The calcite suggests that either the mortar failed along a weaker, carbonated portion of the binder or that secondary calcite precipitated, reinforcing the crack. The presence of the infill suggests the latter and provides a starting point for future investigations into the potential post-pozzolanic remodeling of microcracks in the mortar.

Roman builders' selection of the least altered facies of the Pozzolane Rosse pyroclastic flow, which contains abundant fresh leucite, for the mortar of the Tomb of Caecilia Metella concrete and their placement of the cylindrical structure in an environment open to saturation by ground and surface waters may be the critical factors in the development of the unusual fabrics in the binding phase and the reactive interfacial zones of the tephra components. The monumental structures designed by the contemporaries of Caecilia Metella, the Theater of Pompey, and the Theater of Marcellus mainly use the intermediate alteration facies of Pozzolane Rosse, with leucite crystal fragments more commonly replaced by analcime. Those concretes may have been exposed less frequently to saturation from rainwater and groundwater but were exposed to Tiber River flood waters. That all three structures have survived as functional monuments for 2000 years is a testament to the descriptions of another contemporary, Marcus Vitruvius Pollio, that "the test of excellence of all work can be considered in three parts: fine workmanship (*subtilitate*), magnificence (*magnificentia*), and design (*dispositione*)" (*de Architectura* 5.7.5).

5 | CONCLUSIONS

Mortar samples from the lower sepulchral corridor of the Tomb of Caecilia Metella record exceptionally heterogeneous reactive processes in the binding phase of the cementing matrix and the interfacial zones of Pozzolane Rosse tephra aggregate. The innovative integration of μXRD analyses with spectroscopic methods in micrometer-scale maps provides new insights into the evolution of cementing microstructures and an instructive reference for further study of ancient concrete infrastructure that has remained intact and functional for two millennia.

The analytical results indicate that reaction of tephra with hydrated lime produced pozzolanic C-A-S-H binder but that the tephra components––scoria groundmass, clinopyroxene crystals, and leucite crystals––remain reactive and undergo further changes that contribute to substantial remodeling of the original mortar fabric. Post-pozzolanic mineral cements, such as strätlingite and Al-tobermorite, occur intermittently in the interfacial zones of scoriae and clinopyroxene crystals. The C-A-S-H binder has undergone substantial reconfiguration through incorporation of alumina and potassium apparently derived from pervasive dissolution of leucite crystals. Future investigations will more fully characterize the fine-scale structures and properties of tendril-like C-A-S-H strands with

nanocrystalline preferred orientation and elongate features that split intact C-A-S-H domains. Roman builders' selection of a leucite-rich facies of Pozzolane Rosse tephra as aggregate and the construction of the tomb in an environment with high surface and ground water exposure apparently produced beneficial hydrologic activity and reactivity in the concrete. The ancient material provides an important reference for the long-term behavior of innovative, environmental-friendly concrete infrastructure fabricated with reactive glasses.

ACKNOWLEDGMENTS

We thank Dottoressa Livia Giammichele, Soprintendenza Archeologia di Roma, Parco Archeologico dell'Appia Antica, for assistance with sample collection at the Tomb of Caecilia Metella in 2006. Data acquisition at beamline 12.3.2 at the Advanced Light Source at the Lawrence Berkeley Laboratories was supported by the Director of the Office of Science, Department of Energy, under Contract No. DE-AC02-05CH11231. This research was supported, in part, by a Department of Energy, Advanced Research Projects Agency-Energy (ARPA-E), DE-AR0001139 award to M. D. Jackson at University of Utah. Yao Li, School of Materials Science and Engineering, Chang'an University, Xi'an, Shaanxi P.R. China; Bryony Richards, Energy and Geosciences Institute, Utah; and H.-R. Wenk and T. Teague, Department of Earth and Planetary Sciences, University of California at Berkeley contributed to this research.

AUTHOR CONTRIBUTIONS

Linda M. Seymour and Marie D. Jackson: leader, design, experimentation, analysis, writing, and approval.

Nobumichi Tamura: contributor and experimentation.

Admir Masic: advisor, leader, design, experimentation, analysis, writing, and approval.

ORCID

Marie D. Jackson https://orcid.org/0000-0002-5180-3060

Admir Masic https://orcid.org/0000-0002-8791-175X

REFERENCES

1. Gerding H. *The tomb of Caecilia Metella: Tumulus, tropaeum and theymele* [Ph.D. Dissertation]. Lund (Sweden), Lund University; 2002. 198 p.
2. Paris R, De Vico Fallani M, Mucci A, Marcelli M, De Filippis M, Appia NAV. Il mausoleo di Cecilia Metella e il castrum Caetani. Bull Comm Archeol Comun di Roma. 2000;101:333–44.
3. Rita P. *Via Appia. The Tomb of Cecilia Metella and the Castrum Caetani.*. Milan: Electa; 2000.
4. Coarelli F. *Rome and environs: an archaeological guide*. University of California Press; 2008.
5. Muñoz A. Restauri e nuove indagini su alcuni monumenti della via Appia. Bollettino di Archeologia comunale. 1913;41(2):3–21.
6. Marra F, Freda C, Scarlato P, Taddeucci J, Karner D B, Renne PR, et al. Post-caldera activity in the Alban Hills Volcanic District (Italy): 40Ar/39Ar geochronology and insights into magma evolution. Bull Volcanol. 2003;65(4):227–47.
7. Marra F, Karner DB, Freda C, Gaeta M, Renne PR. Large mafic eruptions at the Alban Hills Volcanic District (Central Italy): chronostratigraphy, petrography and eruptive behavior. J Volcanol Geotherm Res. 2009;179(3–4):217–32. https://doi.org/10.1016/j.jvolgeores.2008.11.009
8. Jackson M, Marra F. Roman Stone Masonry: volcanic foundations of the ancient city. Am J Archaeol. 2006;110(3):403–36.
9. Marra F, Florindo F, Boschi E. The history of glacial terminations from the Tiber River (Rome): insights into glacial forcing mechanisms. Paleooceanography. 2008;23. https://doi.org/10.1029/2007PA001543.
10. Jackson M, Deocampo D, Marra F, Scheetz B. Mid-Pleistocene pozzolanic volcanic ash in ancient Roman concretes. Geoarchaeology. 2010;25(1):36–74. https://doi.org/10.1002/gea.20295
11. Jackson MD, Ciancio Rossetto P, Kosso CK, Buonfiglio M, Marra F. Building materials of the theatre of Marcellus, Rome. Archaeometry. 2011;53(4):728–42. https://doi.org/10.1111/j.1475-4754.2010.00570.x
12. Marra F, D'Ambrosio E, Gaeta M, Mattei M. Petrochemical identification and insights on chronological employment of the volcanic aggregates used in ancient Roman mortars. Archaeometry. 2016;58(2):177–200. https://doi.org/10.1111/arcm.12154
13. van Deman EB. Methods of determining the date of Roman concrete monuments. Am J Archaeol. 1912;16(2):230–51.
14. van Deman EB. Methods of determining the date of Roman concrete monuments (second paper). Am J Archaeol. 1912;16(3):387–432.
15. Marra F, Danti A, Gaeta M. The volcanic aggregate of ancient Roman mortars from the Capitoline Hill: petrographic criteria for identification of Rome's "pozzolans" and historical implications. J Volcanol Geotherm Res. 2015;308:113–26. https://doi.org/10.1016/j.jvolgeores.2015.10.007
16. Packer JE. The Theater of Pompey in Rome: the archeological evidence, the architecture and destruction. Acta Archaeol Artium Hist Pertinentia. 1970;27:9–40. https://doi.org/10.5617/acta.5805
17. Sear F. Vitruvius and Roman theater design. Am J Archaeol. 1990;94(2):249–58.
18. Ciancio Rossetto P, Buonfiglio M. Teatro di Marcello: analisi e riflessione sugli aspetti progettuali e costruttivi. I cantieri Edil di Roma e delle Prov Rom Stud Rom. 2008;56(1–4):3–23.
19. Okoronkwo MU, Glasser FP. Stability of strätlingite in the CASH system. Mater Struct Constr. 2016;49(10):4305–18. https://doi.org/10.1617/s11527-015-0789-x
20. Jackson MD, Landis EN, Brune PF, Vitti M, Chen H, Li Q, et al. Mechanical resilience and cementitious processes in Imperial Roman architectural mortar. Proc Natl Acad Sci U S A. 2014;111(52):18484–9. https://doi.org/10.1073/pnas.1417456111
21. Jackson M, Marra F, Deocampo D, Vella A, Kosso C, Hay R. Geological observations of excavated sand (harenae fossiciae) used as fine aggregate in ancient Roman pozzolanic mortars. J Rom Archaeol. 2007;20:25–51.

22. Jackson MD, Mulcahy SR, Chen H, Li Y, Cappelletti P, Li Q, et al. Phillipsite and Al-tobermorite mineral cements produced through low-temperature water-rock reactions in Roman marine concrete. Am Mineral. 2017;102(7):1435–50. https://doi.org/10.2138/am-2017-5993CCBY
23. Rivard P, Ollivier JP, Ballivy G. Characterization of the ASR rim: application to the Potsdam sandstone. Cem Concr Res. 2002;32(8):1259–67. https://doi.org/10.1016/S0008-8846(02)00765-2
24. Chappex T, Scrivener KL. The effect of aluminum in solution on the dissolution of amorphous silica and its relation to cementitious systems. J Am Ceram Soc. 2013;96(2):592–7. https://doi.org/10.1111/jace.12098
25. Balachandran C, Muñoz JF, Arnold T. Characterization of alkali silica reaction gels using Raman spectroscopy. Cem Concr Res. 2017;92:66–74. https://doi.org/10.1016/j.cemconres.2016.11.018
26. Tamura N, Kunz M, Chen K, Celestre RS, MacDowell AA, Warwick T. A superbend X-ray microdiffraction beamline at the Advanced Light Source. Mater Sci Eng A. 2009;524(1-2):28–32.
27. Stan CV, Tamura N. Synchrotron X-ray microdiffraction and fluorescence imaging of mineral and rock samples. J Vis Exp. 2018;136. https://doi.org/10.3791/57874
28. Tamura N. XMAS: a versatile tool for analyzing synchrotron microdiffraction data. In: Ice G, Barabash B, editors. *Strain dislocation gradients from diffraction*. Vol. 4. Singapore: World Scientific; 2014. p. 125–55. https://doi.org/10.1142/9781908979636_0004
29. Belfiore CM, Fichera GV, La Russa MF, Pezzino A, Ruffolo SA, Galli G, Barca DA, La Russa MF. A multidisciplinary approach for the archaeometric study of pozzolanic aggregate in Roman mortars: the case of Villa dei Quintili (Rome, Italy). Archaeometry. 2015;57(2):269–96. https://doi.org/10.1111/arcm.12085
30. Columbu S, Lisci C, Sitzia F, Lorenzetti G, Lezzerini M, Pagnotta S, et al. Mineralogical, petrographic and physical-mechanical study of Roman construction materials from the Maritime Theatre of Hadrian's Villa (Rome, Italy). Measurement. 2018;127:264–76. https://doi.org/10.1016/j.measurement.2018.05.103
31. Myers RJ, L'Hôpital E, Provis JL, Lothenbach B. Effect of temperature and aluminium on calcium (alumino)silicate hydrate chemistry under equilibrium conditions. Cem Concr Res. 2015;68:83–93. https://doi.org/10.1016/j.cemconres.2014.10.015
32. L'Hôpital E, Lothenbach B, Le Saout G, Kulik D, Scrivener K. Incorporation of aluminium in calcium-silicate-hydrates. Cem Concr Res. 2015;75:91–103. https://doi.org/10.1016/j.cemconres.2015.04.007
33. Sun GK, Young JF, Kirkpatrick RJ. The role of Al in C-S-H: NMR, XRD, and compositional results for precipitated samples. Cem Concr Res. 2006;36(1):18–29. https://doi.org/10.1016/j.cemconres.2005.03.002
34. Lafuente B, Downs RT, Yang H, Stone N. The power of databases: the RRUFF project. In: Armbruster T, Danisi RM, editors. *Highlights in mineralogical crystallography*. Berlin: W. De Gruyter; 2015. p. 1–30.
35. Ortaboy S, Li J, Geng G, Myers RJ, Monteiro PJM, Maboudian R, et al. Effects of CO_2 and temperature on the structure and chemistry of C-(A-)S-H investigated by Raman spectroscopy. RSC Adv. 2017;7(77):48925–33. https://doi.org/10.1039/c7ra07266j
36. Taylor HFW. Tobermorite, jennite, and cement gel. Kristallographie-Crystalline Materials. 1992;202(1–4):41–50.
37. Jackson MD, Moon J, Gotti E, Taylor R, Chae SR, Kunz M, et al. Material and elastic properties of Al-tobermorite in ancient Roman seawater concrete. J Am Ceram Soc. 2013;96(8):2598–606. https://doi.org/10.1111/jace.12407
38. Jackson MD, Chae SR, Mulcahy SR, Meral C, Taylor R, Li P, et al. Unlocking the secrets of Al-tobermorite in Roman seawater concrete. Am Mineral. 2013;98(10):1669–87. https://doi.org/10.2138/am.2013.4484
39. Abdolhosseini Qomi MJ, Ulm FJ, Pellenq RJM. Evidence on the dual nature of aluminum in the calcium-silicate-hydrates based on atomistic simulations. J Am Ceram Soc. 2012;95(3):1128–37. https://doi.org/10.1111/j.1551-2916.2011.05058.x
40. Pellenq RJ-M, Kushima A, Shahsavari R, Van Vliet KJ, Buehler MJ, Yip S, et al. A realistic molecular model of cement hydrates. Proc Natl Acad Sci U S A [Internet]. 2009;106(38):16102–7. https://doi.org/10.1073/pnas.0902180106
41. Myers RJ, L'Hôpital E, Provis JL, Lothenbach B. Composition–solubility–structure relationships in calcium (alkali) aluminosilicate hydrate (C-(N, K-)A-S-H). Dalt Trans. 2015;44(30):13530–44. https://doi.org/10.1039/c5dt01124h
42. Hong S-Y, Glasser FP. Alkali sorption by C-S-H and C-A-S-H gels: part II. Role of alumina. Cem Concr Res. 2002;32(7):1101–11. https://doi.org/10.1016/S0008-8846(02)00753-6
43. Dufresne, A, Arayro, J, Zhou, T, Ioannidou, K, Ulm, F-J, Pellenq, R, et al. Atomistic and mesoscale simulation of sodium and potassium adsorption in cement paste. J Chem Phys. 2018;149:074705. https://doi.org/10.1063/1.5042755
44. Richardson, I.G., Groves, G.W. Microstructure and microanalysis of hardened ordinary Portland cement pastes. J Mat Sci. 1993;28:265–77. https://doi.org/10.1007/BF00349061
45. Provis, J.L., Palomo, A, Shi, C. Advances in understanding alkali-activated materials. Cem Concr Res. 2015;78:110–25. https://doi.org/10.1016/j.cemconres.2015.04.013
46. Jackson, M. D., Zhang Y., Chen H., Moon J. *Autogenous mineral textures in micropores and microcracks Roman architectural concrete, Markets of Trajan, Rome*. RILEM Proceedings 14th International Conference on Durability of Building Materials and Components. Universiteit Gent, Gent, Belgium, 29–31 May 2017.
47. Black L. Raman spectroscopy of cementitious materials. In Yarwood J, Douthwaite R, Duckett S, editors. *Spectroscopic properties of inorganic and organometallic compounds*. 2009. p. 72–127. https://doi.org/10.1039/b715000h
48. Königsberger M, Pichler B, Hellmich C. Micromechanics of ITZ–aggregate interaction in concrete part I: stress concentration. J Am Ceram Soc. 2014;97(2):535–42. https://doi.org/10.1111/jace.12591
49. Königsberger M, Pichler B, Hellmich C. Micromechanics of ITZ–aggregate interaction in concrete part II: strength upscaling. J Am Ceram Soc. 2014;97(2):543–51. https://doi.org/10.1111/jace.12606
50. Prokopski G, Halbiniak J. Interfacial transition zone in cementitious materials. Cem Concr Res. 2000;30(4):579–83. https://doi.org/10.1016/S0008-8846(00)00210-6
51. Ponce JM, Batic OR. Different manifestations of the alkali-silica reaction in concrete according to the reaction kinetics of the reactive aggregate. Cem Concr Res. 2006;36(6):1148–56. https://doi.org/10.1016/j.cemconres.2005.12.022

52. ASTM International. ASTM C1260 - 14 Standard Test Method for Potential Alkali Reactivity of Aggregates (Mortar-Bar Method). 2014.
53. Landis EN, Zhang T, Nagy EN, Nagy G, Franklin WR. Cracking, damage and fracture in four dimensions. Mater Struct. 2007;40(4):357–64. https://doi.org/10.1617/s11527-006-9145-5
54. Kuroda M, Watanabe T, Terashi N. Increase of bond strength at interfacial transition zone by the use of fly ash. Cem Concr Res. 2000;30(2):253–8. https://doi.org/10.1016/S0008-8846(99)00241-0
55. Duan P, Shui Z, Chen W, Shen C. Effects of metakaolin, silica fume and slag on pore structure, interfacial transition zone and compressive strength of concrete. Constr Build Mater. 2013;44:1–6. https://doi.org/10.1016/j.conbuildmat.2013.02.075
56. Gao JM, Qian CX, Liu HF, Wang B, Li L. ITZ microstructure of concrete containing GGBS. Cem Concr Res. 2005;35(7):1299–304. https://doi.org/10.1016/j.cemconres.2004.06.042
57. Snellings R, Mertens G, Elsen J. Supplementary cementitious materials. Rev Mineral Geochem. 2012;74(1):211–78. https://doi.org/10.2138/rmg.2012.74.6
58. Luke K, Lachowski E. Internal composition of 20-year-old fly ash and slag-blended ordinary Portland cement pastes. J Am Ceram Soc. 2008;91(12):4084–92. https://doi.org/10.1111/j.1551-2916.2008.02783.x
59. Maruyama I, Rymeš J, Aili A, Sawada S, Kontani O, Ueda S, et al. Long-term use of modern Portland cement concrete: the impact of Al-tobermorite formation. Mater Des [Internet]. 2021;198:109297. https://doi.org/10.1016/j.matdes.2020.109297

How to cite this article: Seymour LM, Tamura N, Jackson MD, Masic A. Reactive binder and aggregate interfacial zones in the mortar of Tomb of Caecilia Metella concrete, 1C BCE, Rome. J Am Ceram Soc. 2022;105:1503–1518. https://doi.org/10.1111/jace.18133